地学雑誌　Journal of Geography (Chigaku Zasshi)　135 (4) 359–380 2026　doi:10.5026/jgeography.135.359

Diffusive Seismicity Preceding an *M* 6.6 West-off Noto Peninsula (Japan) Earthquake on 26 November 2024

Kazuhiro ITADERA*, Masaki NAKAMURA, Tamotsu AKETAGAWA***, Fuyuki HIROSE** and Akio YOSHIDA***

[Received 16 October, 2025; Accepted 14 May, 2026]

Abstract

We investigated seismicity preceding an M 6.6 earthquake that occurred west-off Noto Peninsula on 26 November 2024 (Japan Standard Time), using a hypocenter catalog re-located based on waveform correlation. The preceding seismicity was divided into four periods, Period 1: (from the last 10 days of January until February), Period 2: (from March until late September), Period 3: (from late September until late October), and Period 4: (from 1st November until the occurrence of the M 6.6 earthquake). Short-term activities of several hours to half a day were observed in Period 1, while comparatively long-lasting activities of about two weeks were observed in Periods 3 and 4. In each of these activities, diffusive hypocenter migration was observed. Diffusivity was estimated at approximately 1 m^2/s for the activities in Period 1, and 0.1 m^2/s, a one-order smaller value, for the activities in Periods 3 and 4. Based on the value of diffusivity and relatively short duration, we consider the diffusive activities observed in Period 1 to be linked to a slow fault-slip, an assumption that is supported by a fractal dimension of the hypocenter distribution that is nearly 2. On the other hand, the diffusive activities in Periods 3 and 4 may have been caused by the intrusion of fluids into the fracture zone because the diffusivity is almost the same as that observed in the swarm activity preceding the 2024 Noto Peninsula earthquake (M 7.6), which is considered to have originated by upward fluid migration. The b values in the Gutenberg-Richter law for activities in Period 1 and in Periods 3 and 4 were 0.75 ± 0.07 and 0.53 ± 0.06, respectively. These low b values, especially in Periods 3 and 4, indicate that the area was highly stressed. The seismograms of the M 6.6 west-off Noto Peninsula earthquake show that amplitude of the P-wave was small initially and grew gradually. We postulate that the fault motion first spread out in the area of the preceding seismic activity that was highly stressed and whose overall fault strength had been weakened by the intrusion of fluids. Thereafter, the fault motion extended along a pre-existing fault which finally resulted in the M 6.6 earthquake.

Key words: west-off Noto Peninsula earthquake, diffusive seismicity, waveform correlation, b value, fractal dimension

* Center for Integrated Research and Education of Natural Hazards, Shizuoka University, Shizuoka, 422-4502, Japan
** Meteorological Research Institute, Tsukuba, 305-0052, Japan
*** Osaka District Meteorological Observatory, Osaka, 540-0008, Japan

I. Introduction

Notable seismic activities were observed prior to a magnitude (*M*) 6.6 earthquake that occurred west-off the Noto Peninsula, Japan on 26 November 2024 (Japan Standard Time). We investigated characteristics of the spatio-temporal distribution of earthquakes in the preceding activities. Much effort has been exerted to distinguish precursory seismicity, which results in the occurrence of a large earthquake, during which it has been reported that earthquake migration or diffusion are observed (Kato *et al*., 2012; Chen and Shearer, 2013; Ruiz *et al*., 2014; Sugan *et al*., 2014; Cabrera *et al*., 2022; Yoshida *et al*., 2023), the *b* value of the Gutenberg -Richter law is low (Schorlemmer *et al*., 2004; Nanjo *et al*., 2012; Gulia and Wiemer, 2019; Nanjo and Yoshida, 2021; Shimbaru and Yoshida, 2021), and foreshocks are likely to be located in the proximity of the mainshock focus (Hamada, 1987; Yoshida and Hamada, 1991; Maeda, 1996). In this study, we report that the activity preceding the *M* 6.6 earthquake showed all these characteristics.

The fault of the *M* 7.6 Noto Peninsula earthquake on 1 January 2024, which consisted of multiple segments, extended over 150 km overall. The hypocenter of the *M* 6.6 earthquake was located 20 km west of the westernmost segment of the 2024 Noto Peninsula earthquake (Fig. 1). Centroid moment tensor solution of the *M* 6.6 earthquake indicated a reverse fault along the east-west pressure axis (Japan Meteorological Agency, 2024). Toda and Stein (2024) calculated change in the Coulomb Failure Function (ΔCFF) brought about by fault motion in the 2024 Noto Peninsula earthquake, and showed that the *M* 6.6 earthquake was located in region where ΔCFF for reverse fault motion increased along an east-west pressure axis.

To investigate the characteristics of the precursory activity, we used relocated hypocenters based on seismic waveform correlation. In the following section, we explain how we constructed the hypocenter catalog, then briefly point out some easily visible features of the hypocenter distribution of precursory activities and aftershocks of the *M* 6.6 earthquake. In the latter half of section II, we assess the problem of the re-located hypocenter of the *M* 6.6 earthquake, which was determined far west of the area of the precursory activity. Seismograms of the *M* 6.6 earthquake at each observation site show that it was difficult to detect the first arrival time of the S-wave due to overlapping large-amplitude P-waves that appeared later. This situation very likely affected the calculated location of the *M* 6.6 earthquake because, during the re-locating procedure, hypocenters were determined based on P- and S-wave arrival times selected by the Japan Meteorological Agency (JMA) staff. By comparing the arrival times of P-waves at observation sites in and around the Noto Peninsula for three earthquakes, the location of the hypocenter of the *M* 6.6 earthquake—relative to the hypocenters of the other two earthquakes and to the area of precursory activity—was estimated.

In section III, diffusion of earthquake hypocenters, as well as some notable features of their spatial distribution, are described. In section IV, the *b* values and fractal dimensions of the precursory activities are calculated, accompanied by a discussion of the results' implications. Then, combining that discussion with the diffusive features of the earthquake hypocenters and characteristics of their spatial distribution, we postulate what may have occurred before and at the beginning of the fault motion of the *M* 6.6 earthquake in the area around the focus. Results of these analyses and discussion are summarized in section V.

II. Data and methods

In this study, we analyzed the spatio-temporal distribution of earthquakes that occurred after the *M* 7.3 2024 Noto Peninsula earthquake in the area denoted by the green rectangle in Fig. 1. The JMA catalog contains 5,084 earthquakes with *M* 1.0 or larger in the period from January 2024 until March 2025. First, we relocated the hypocenters by using P- and S-wave arrival times selected by the JMA at stations shown in

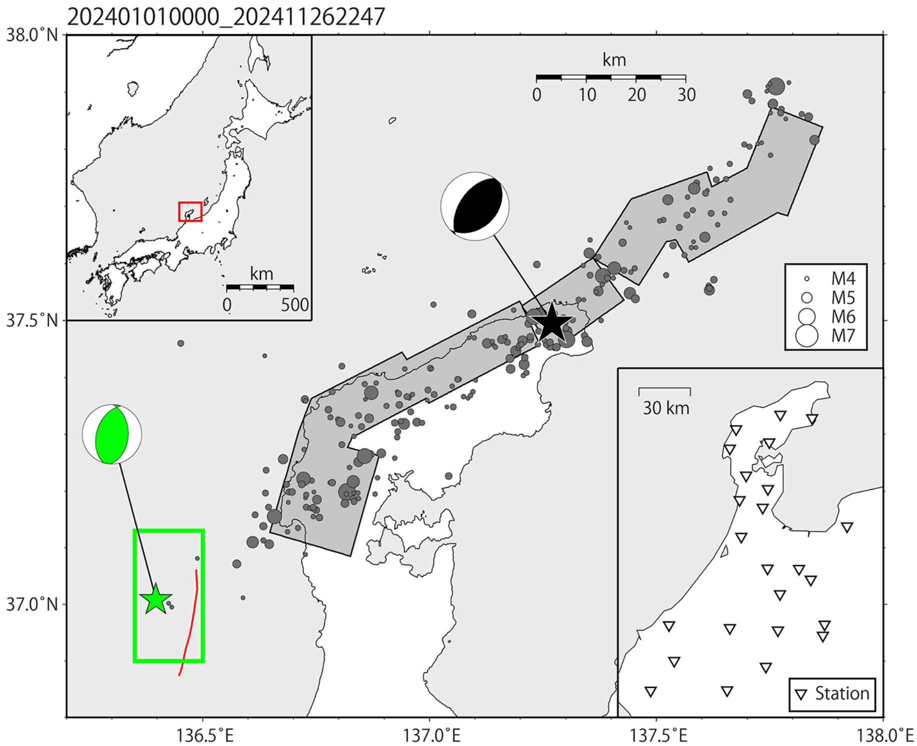

Fig. 1 Epicenters of an *M* 6.6 earthquake on 26 November 2024 (green star) and the *M* 7.6 Noto Peninsula earthquake on 1 January 2024 (black star). Small black circles show epicenters of earthquakes that occurred in the period between the two earthquakes. Centroid moment tensor solutions of the *M* 7.6 and the *M* 6.6 earthquake on 26 November were taken from JMA (2024). The shaded rectangular area shows fault model of the *M* 7.6 Noto Peninsula earthquake was taken from by Toda and Stein (2024). Red line indicates the western Hakui-oki fault. Inset on the left top shows the location of the Noto region in Japan, and that on the right bottom shows location points of seismographs whose seismic data were used in producing the relocated hypocenter catalog.

Fig. 1. Next, based on the relocated hypocenters, we obtained corrections of arrival times for each station. Then, taking the arrival-time corrections into consideration, we relocated the hypocenters. Finally, we calculated relative location, using waveform cross correlation, by adopting the GrowClust algorithm (Trugman and Shearer, 2017), which is essentially based on the event-pair double difference method (Waldhauser and Ellsworth, 2000). In the procedure, we used the xcorr pick correction of ObsPy (Beyreuther *et al*., 2010), and after applying Deep Denoiser (Zhu *et al*., 2019), we pre-processed band-pass filters of 2–8 Hz. We obtained time differences of the P-wave arrival times from the vertical component and those of the S-wave arrival times from the transverse component. The numbers of P- and S-wave differential times were 10,134,716 and 4,579,902, respectively. We used 2,662,573 event pairs with a correlation coefficient ≧ 0.6, and the 1-D velocity model JMA 2001 (Ueno *et al*., 2002) to calculate hypocenter. We obtained a hypocenter catalog of 4,867 earthquakes that were used in our analysis. Horizontal and vertical error distributions of the relocated hypocenters are shown in Electronic Appendix 1.

Fig. 2 shows the seismicity before the *M* 6.6 earthquake on 26 November 2024. Seismicity became active three times. We investigated the spatio-temporal features of the preceding seismicity by dividing it into four periods, Period 1:

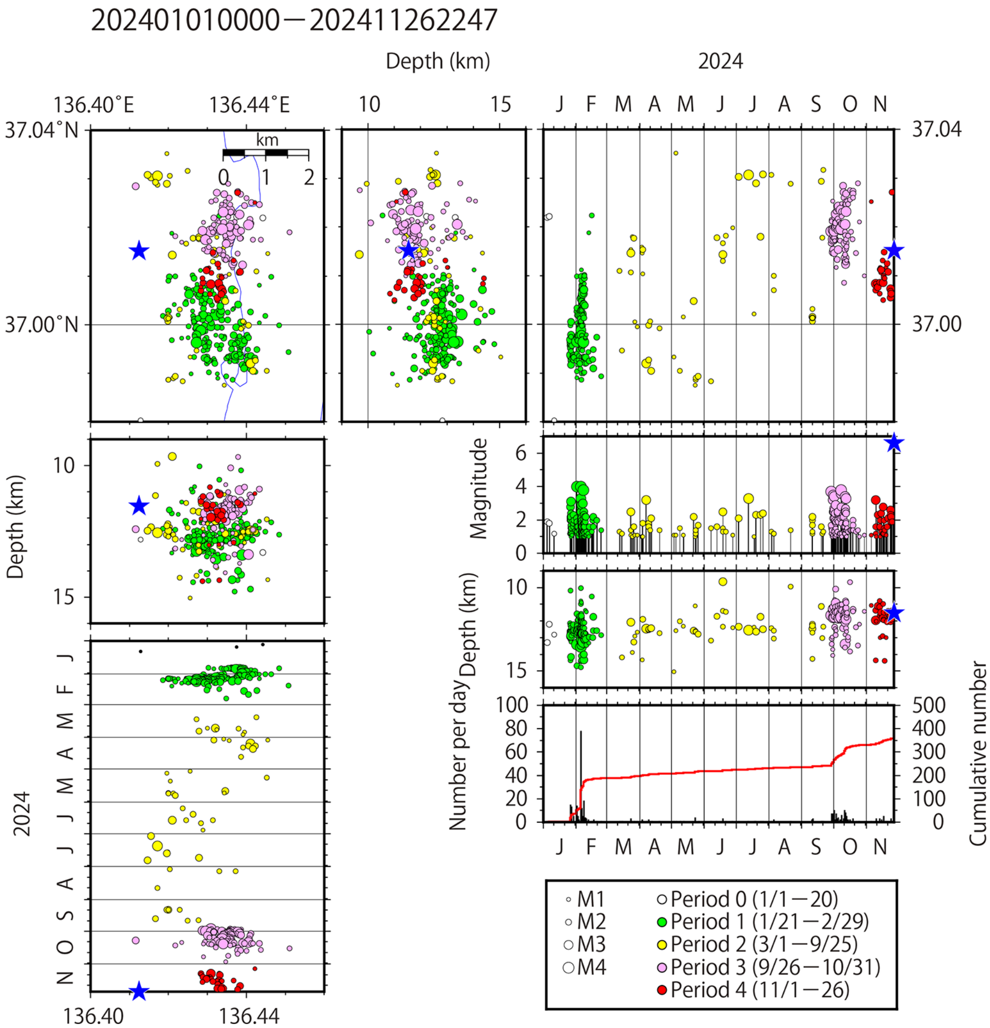

Fig. 2　Epicentral distribution, cross section and space-time variation in the north-south direction (upper panel) and those in the east-west direction (bottom left panel), and magnitude-time diagram, change in the depth, as well as daily and cumulative number of earthquakes (bottom right panel) for the precursory activity. Earthquakes in Periods 1, 2, 3, and 4 are shown in green, yellow, pink, and red, respectively. Blue star shows the hypocenter of the *M* 6.6 earthquake. The area of the map of the epicentral distribution corresponds to the square delineated by red lines in Fig. 3. The blue line in the map indicates the 200-meter seafloor contour.

from 21 January until 29 February, Period 2: from 1 March until 25 September, Period 3: from 26 September until 31 October, and Period 4: from 1 November until the occurrence of the *M* 6.6 earthquake. The epicentral distribution, where events in each period are plotted by different colors, reveals that earthquakes in Period 1 occurred in the southern part of the area of the preceding activity, while earthquakes in Periods 3 and 4 occurred in its northern part. The epicentral area of earthquakes in Period 4 appears to overlap with the northern part of the area of activity in Period 1. However, the depths of earthquakes in Periods 1 and 4 were different. Seismicity in Period 2 was relatively quiet. Features of the space-time distribution of earthquakes in each Period are described in detail in section III.

Aftershocks of the M 6.6 earthquake were distributed in a north-south direction and hypocentral depths mostly ranged from 10 to 15 km, shallower in the northern part and slightly deeper in the central part. A feature of the east-west cross sections (A), (B), (C) is that the depths of aftershocks tended to become shallower in the east, although this tendency was not clear in the southernmost section (D). From the depth distribution of these aftershocks, the fault plane of the M 6.6 earthquake is thought to have declined to the west, which is consistent from a macro perspective, with the reverse fault mechanism of the earthquake having an east-west pressure axis (JMA, 2024). Extension of the distribution of aftershocks to the shallower direction crosses the seabed near the western Hakui-oki active fault (cf. Fig. 1).

As shown in Figs. 3 and 4, the hypocenter of the M 6.6 earthquake was determined in the western end of the aftershock activity, away from the area of the preceding activity. The hypocenter of the M 6.6 earthquake in the JMA catalog is located 1.52 km further west and the depth (7.64 km) is 4.08 km shallower than the relocated hypocenter. Next, we discuss some problems related to the location of the hypocenter of the M 6.6 earthquake.

As described in the first paragraph of this section, in the procedure used to create the relocated hypocenter catalog, we first calculated provisional hypocenters by using the arrival times of P- and S-waves detected by JMA staff at observation sites shown in Fig. 1. Electronic Appendix 2a shows seismograms of the M 6.6 earthquake at TOGI, HAKUI, SHIKA, and NANAO stations in the Noto Peninsula that are located to the east of the focus, and at KAGA station, which is located to the south. The same figure also indicates the appearance times of P- and S-waves as detected by JMA staff. Electronic Appendix 2b and c are the same as Electronic Appendix 2a, but corresponding to an M 3.2 earthquake on 9 November, and an M 4.0 earthquake on 30 November, respectively. Note that the amplitude of the P-wave of the M 6.6 earthquake was not large initially, but gradually enlarged and the developing P-waves overlapped with small-amplitude S-waves. This overlap made it difficult to recognize the first arrival of the S-wave. The difficulty in detecting the start of the S-wave of the M 6.6 earthquake is also suggested by the temporal order of the arrival times selected for the S-waves at TOGI, HAKUI, and SHIKA stations, which differ from the order for the P-wave. Locations of the observation sites in the Noto Peninsula correspond to the direction of the maximum pressure axis in the fault motion for which amplitudes of the S-wave tend to become relatively small. This situation might be another explanation for the difficulty reading the first S-wave. Horizontal error of the hypocenter of the M 6.6 earthquake relocated by GrowClust is 602 m, which is much larger than 425 m, the median of the horizontal errors for all the relocated hypocenters. This also indicates that the relocated hypocenter of the M 6.6 earthquake is suspect. When the start of the S-waves is detected later than the true arrival times, the reading makes the S-P times larger, and the hypocenter is determined to be further west from the stations in the Noto Peninsula. We attempted to estimate the location of the hypocenter of the M 6.6 earthquake not using readings of the arrival times of the S-wave in seismograms.

The KAGA station is located due south of the focal region of the west-off Noto Peninsula earthquake (Fig. 4). As hypocenters of an M 3.2 event on 9 November 2024 and an M 4.0 event on 30 November 2024 are located at nearly the same latitude (Fig. 5), it is assumed that the travel time of the P-wave to the KAGA station is almost the same for the two earthquakes. However, the travel time of the P-wave at each station in the Noto Peninsula should be different in these two events, i.e., the travel time should be larger for the M 4.0 event whose hypocenter is located further west. Table 1 shows differences of the P-wave arrival times (DPAT) between KAGA and each station in the Noto Peninsula for the above-mentioned M 3.2 and

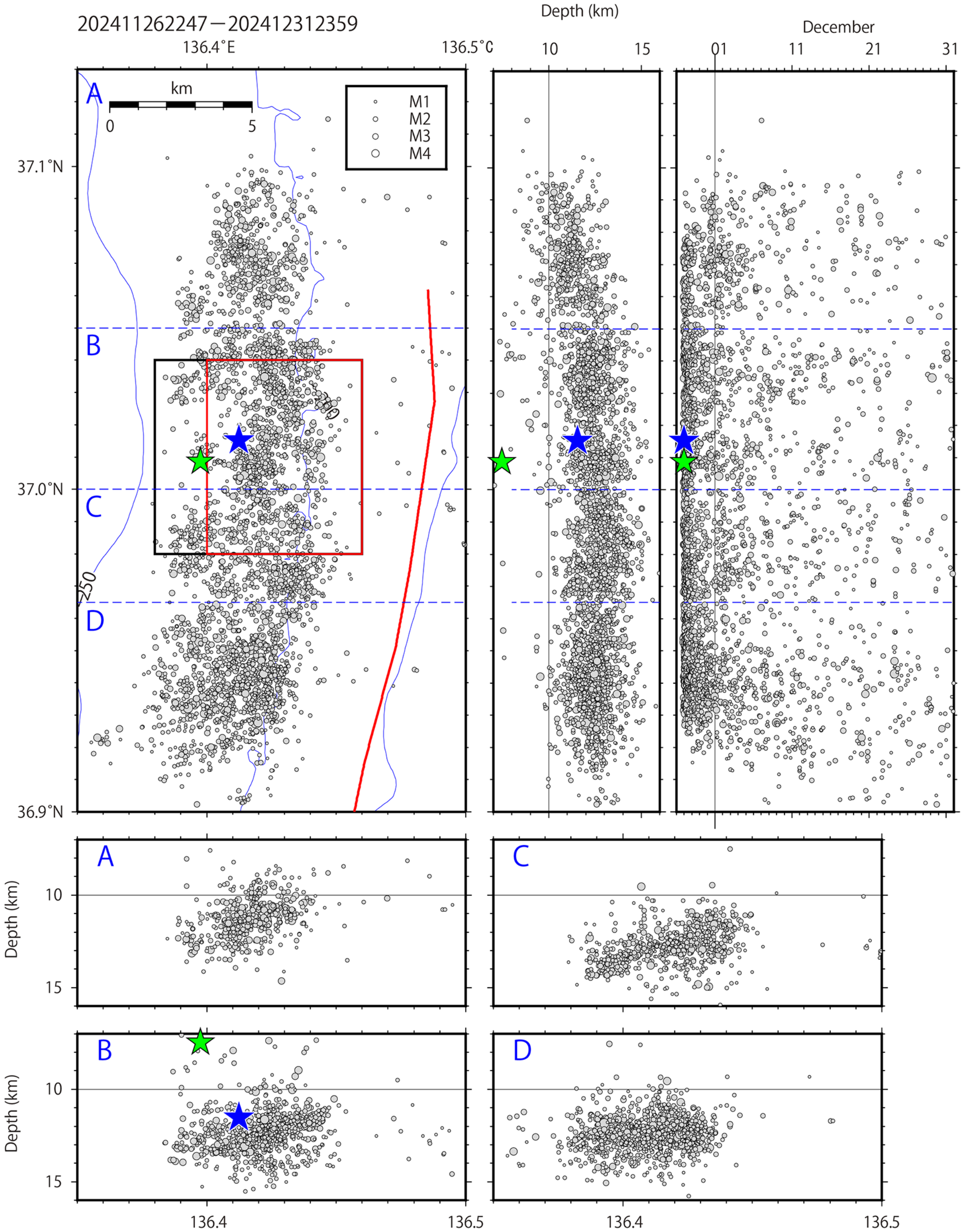

Fig. 3 Upper panel: Epicentral distribution, north-south cross section and space-time distribution of aftershocks in the period from the occurrence of the M 6.6 earthquake on 26 November until 31 December. Lower panel: Cross sections of aftershocks in the east-west direction. Blue and green stars represent the hypocenter of the M 6.6 earthquake in the relocated catalog and in the JMA catalog, respectively. The squares delineated by red and black lines indicate the area of the precursory activity shown in Fig. 2 and the area of the map of Fig. 5, respectively.

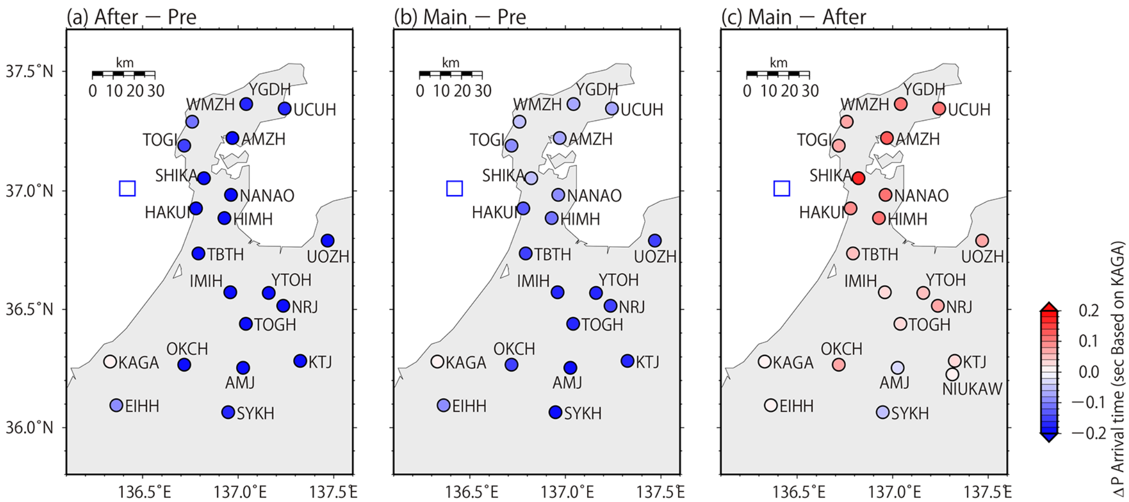

Fig. 4 (a) Difference in DPAT between the *M* 4.0 event on 30 November and the *M* 3.2 event on 9 November, (b) between the *M* 6.6 earthquake and the *M* 3.2 event, and (c) between the *M* 6.6 earthquake and the *M* 4.0 event, at stations around the Noto Peninsula. DPAT represents Difference of P-wave Arrival Time between KAGA and any other stations; i.e., P-wave Arrival Time at KAGA minus that at any other stations. Note that the difference is a negative value for case (b), i.e., DPAT for the *M* 3.2 event is larger than that for the *M* 6.6 event at almost all stations and a positive value at almost all stations for case (c), indicating that the hypocenter of the *M* 6.6 earthquake is located west of the *M* 3.2 event and east of the *M* 4.0 event.

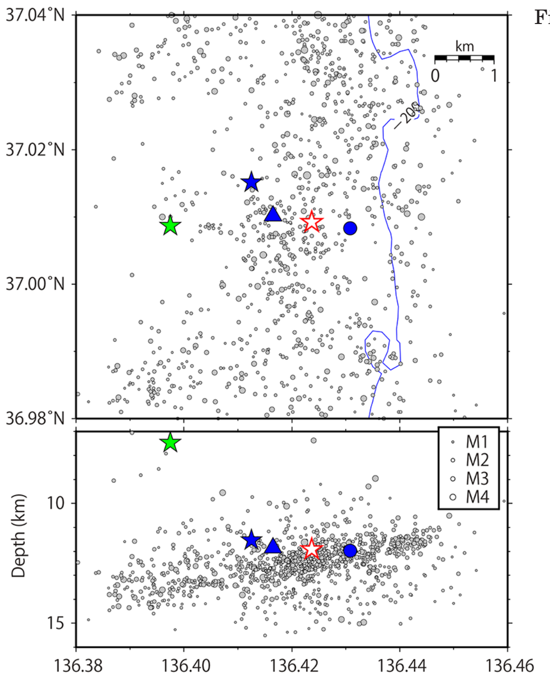

Fig. 5 Relative locations of the *M* 6.6 mainshock on 26 November (blue star), an *M* 3.2 event on 9 November (blue circle), and an *M* 4.0 event on 30 November (blue triangle) based on the relocated catalog. The green star shows the location of the *M* 6.6 mainshock based on the JMA catalog. The red star indicates the location of the hypocenter of the *M* 6.6 earthquake inferred from differences in DPAT between the *M* 6.6, *M* 3.2, and *M* 4.0 earthquakes at stations in and around the Noto Peninsula (cf. Fig. 4). The map area corresponds to the black square in the epicentral map of Fig. 3.

M 4.0 events and the *M* 6.6 earthquake. Note that DPAT should become smaller for the event with a more western hypocenter. Fig. 4a shows differences of the DPAT values between the *M* 3.2 event and the *M* 4.0 event at each station in color code, where the DPAT values for the *M* 3.2 event were subtracted from the DPAT values for the *M* 4.0 event. From Fig. 4a it is observed that the DPAT for the *M* 4.0 event on 30 November is smaller than that for the *M* 3.2 event at almost all stations, coinciding with their relative location of the hypocenter of the *M* 4.0 event, which is located west of the hypo-

Table 1　P-wave and S-wave arrival times and DPAT at stations shown in Fig. 1 for the M 3.2 earthquake on 9 November, the M 6.6 earthquake on 26 November, and the M 4.0 earthquake on 30 November, where DPAT indicates differences of P arrival times between Kaga and each of the other stations.

Station	9-Nov.-24 23:43 M 3.2						26-Nov.-24 22:47 M 6.6						30-Nov.-24 10:22 M 4.0					
	hour	P-arrival		S-arrival		D.P.A.T.	hour	P-arrival		S-arrival		D.P.A.T.	hour	P-arrival		S-arrival		D.P.A.T.
		min	sec	min	sec	sec		min	sec	min	sec	sec		min	sec	min	sec	sec
TOGI	23	43	50.90	43	55.11	8.40	22	47	9.17	47	13.99	8.31	10	22	13.50	22	17.45	8.25
HAKUI	23	43	51.03	43	55.56	8.27	22	47	9.35	47	13.62	8.13	10	22	13.70	22	18.38	8.05
SHIKA	23	43	51.36	43	55.82	7.94	22	47	9.59	47	14.48	7.89	10	22	14.03	22	18.69	7.72
WMZH	23	43	52.76	43	58.32	6.54	22	47	10.99	47	16.69	6.49	10	22	15.33	22	21.06	6.42
TBTH	23	43	52.76	43	58.58	6.54	22	47	11.09	47	17.11	6.39	10	22	15.41	22	21.21	6.34
HIMH	23	43	53.08	43	58.80	6.22	22	47	11.38	47	17.83	6.10	10	22	15.75	22	21.69	6.00
NANAO	23	43	53.29	43	59.30	6.01	22	47	11.56	47	18.76	5.92	10	22	15.94	22	22.21	5.81
AMZH	23	43	54.45	44	1.20	4.85	22	47	12.70	47	19.82	4.78	10	22	17.10	22	23.95	4.65
YGDH	23	43	56.61	44	5.01	2.69	22	47	14.86	47	23.60	2.62	10	22	19.23	22	27.88	2.52
IMIH	23	43	57.07	44	5.67	2.23	22	47	15.43			2.05	10	22	19.72	22	28.71	2.03
UCUH	23	43	59.07	44	9.28	0.23	22	47	17.32	47	28.11	0.16	10	22	21.70	22	32.14	0.05
YTOH	23	43	59.15		0.00	0.15	22	47	17.50	47	27.82	−0.02	10	22	21.81	22	32.39	−0.06
TOGH	23	43	59.16	44	9.37	0.14	22	47	17.52	47	28.26	−0.04	10	22	21.82	22	32.14	−0.07
KAGA	23	43	59.30	44	9.25	0.00	22	47	17.48			0.00	10	22	21.75	22	31.80	0.00
OKCH	23	43	59.69	44	10.16	−0.39	22	47	18.02	47	29.16	−0.54	10	22	22.35	22	32.80	−0.60
NRJ	23	44	0.22	44	11.26	−0.92	22	47	18.55	47	30.98	−1.07	10	22	22.88	22	33.99	−1.13
UOZH	23	44	1.33			−2.03	22	47	19.66	47	31.61	−2.18	10	22	24.00	22	36.26	−2.25
AMJ	23	44	1.57			−2.27	22	47	19.97			−2.49	10	22	24.21	22	36.39	−2.46
EIHH	23	44	1.99	44	14.01	−2.69	22	47	20.26	47	32.92	−2.78	10	22	24.54	22	36.71	−2.79
KTJ	23	44	3.89			−4.59	22	47	22.25	47	37.54	−4.77	10	22	26.54	22	40.51	−4.79
SYKH	23	44	4.30	44	17.95	−5.00	22	47	22.71			−5.23	10	22	26.93	22	40.67	−5.18
NIUKAW	23						22	47	22.81	47	38.50	−5.33	10	22	27.09	22	41.27	−5.34

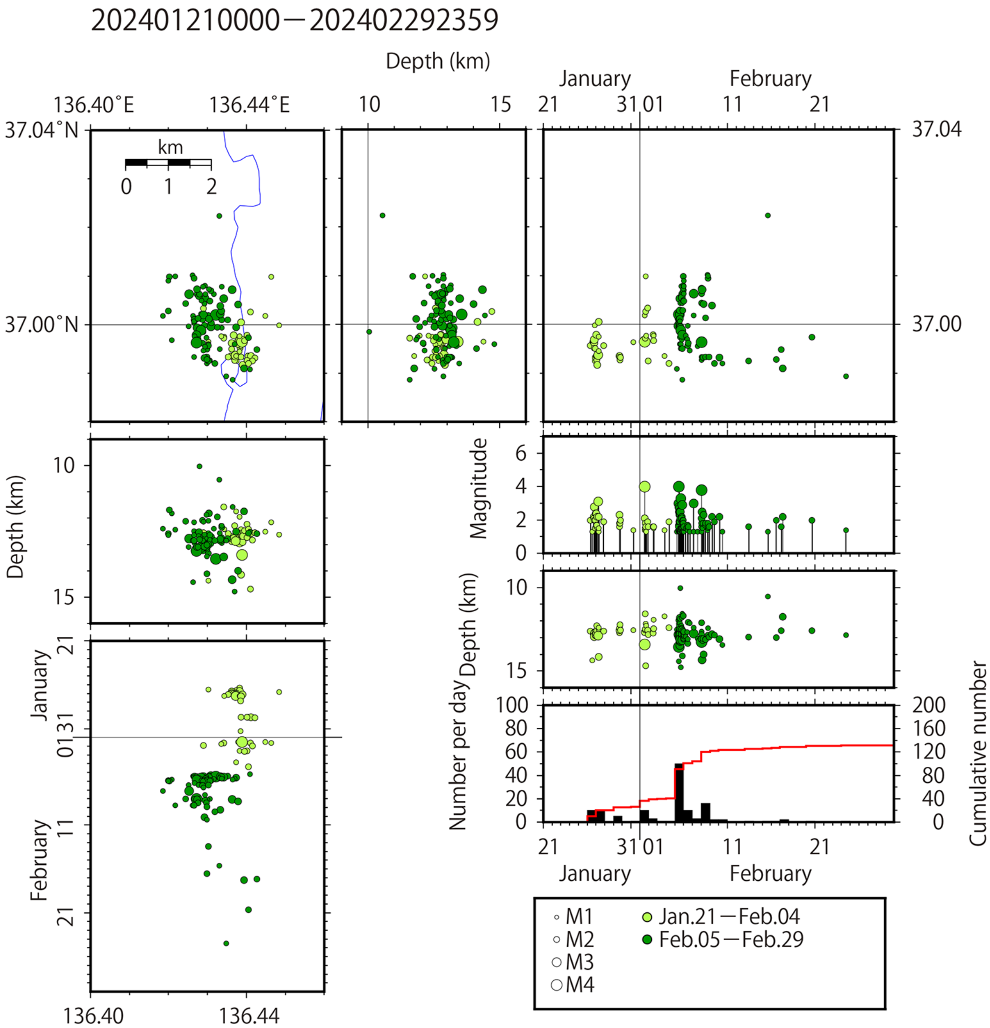

Fig. 6 Same as Fig. 2, but for Period 1. Earthquakes in the former half period and those in the latter half period are plotted in light green and deep green, respectively.

center of the M 3.2 event. Similarly, when DPAT for the M 6.6 earthquake is compared to DPAT for the M 3.2 event, the former is smaller at almost all stations (Fig. 4b). However, it is notable that DPAT for the M 6.6 earthquake is larger than DPAT for the M 4.0 event at almost all stations (Fig. 4c). Figs. 4b and 4c indicate that the hypocenter of the M 6.6 earthquake was located east of the M 4.0 event and west of the M 3.2 event. The star in Fig. 5 shows the location of the M 6.6 earthquake inferred from the comparison of the DPAT values for the M 6.6 earthquake with those for the M 3.2 and M 4.0 earthquakes.

III. Precursory activity in each Period

1) Activity in Period 1

As is shown in Fig. 6, earthquakes in Period 1 occurred overall in an elliptic area of about 3 km × 2 km with its major axis running in a northwest-southeast direction. The activity until 4 February occurred in the southeastern part and that after 5 February occurred in the northwestern part. Depths of the earthquakes

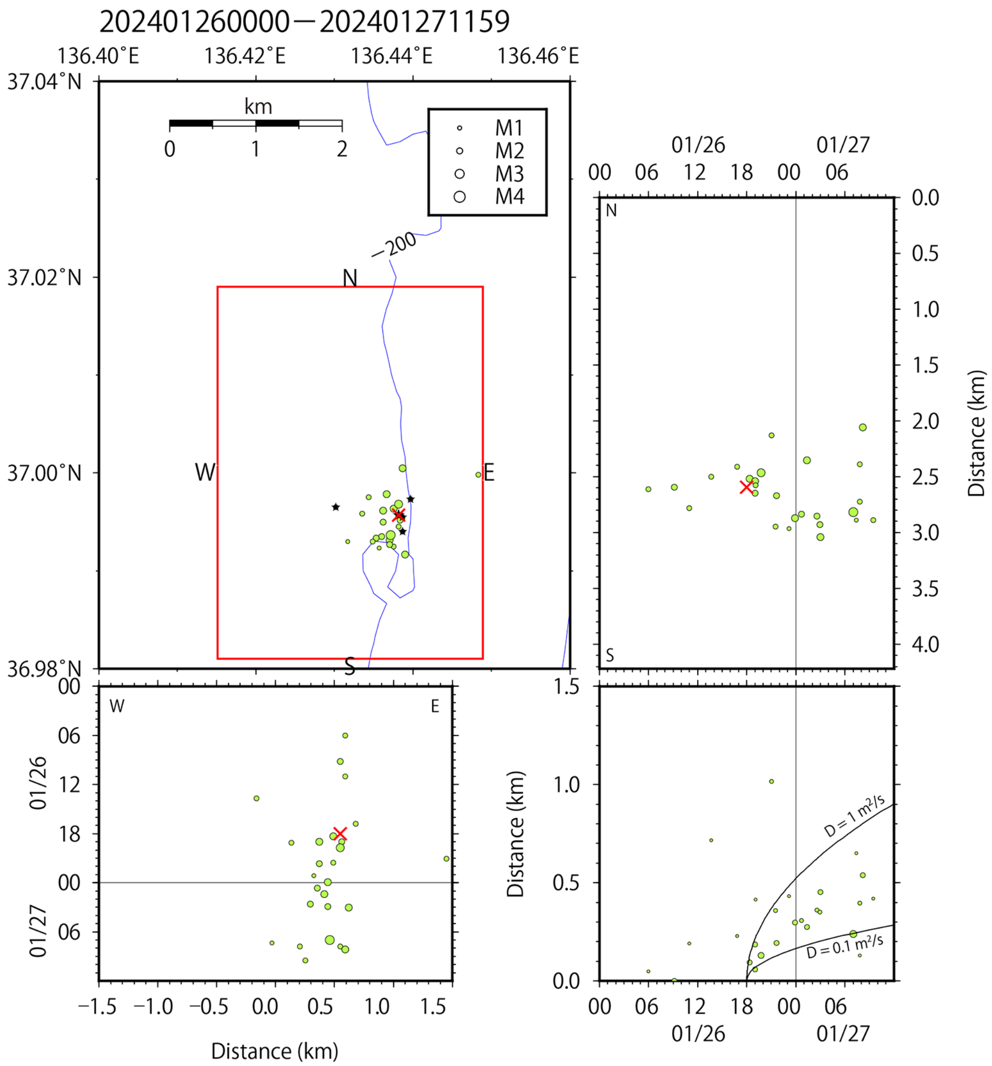

Fig. 7　Epicentral distribution and space-time variation in the north-south direction and in the east-west direction for the activity on 26–27 January. Bottom right panel is a graph where epicentral distances of earthquakes from the cross mark on the epicenter map are plotted against their occurrence times. Curves represent an isotropic pore-fluid pressure diffusion model proposed by Shapiro *et al*. (1997). The location of the cross mark was determined to be nearly the central point in the epicentral distribution of the first five earthquakes after 6 p.m. (plotted as black stars), also referring to the north-south and east-west space-time distributions of the activity. The red rectangle corresponds to that in Fig. 3.

were mostly in the range of 12–14 km. From the space-time distribution and the magnitude-time diagram (M-T diagram), it can be appreciated that swarm-like activity occurred on 26–27 January, and on 5–6 February.

Fig. 7 shows an epicentral map of earthquakes on 26–27 January, a space-time distribution in the north-south and east-west directions, and a diagram where epicentral distances of earthquakes from the cross mark on the map are plotted against their occurrence times. Applying an isotropic pore-fluid pressure diffusion model proposed by Shapiro *et al*. (1997), it was estimated that the activity diffused at a diffu-

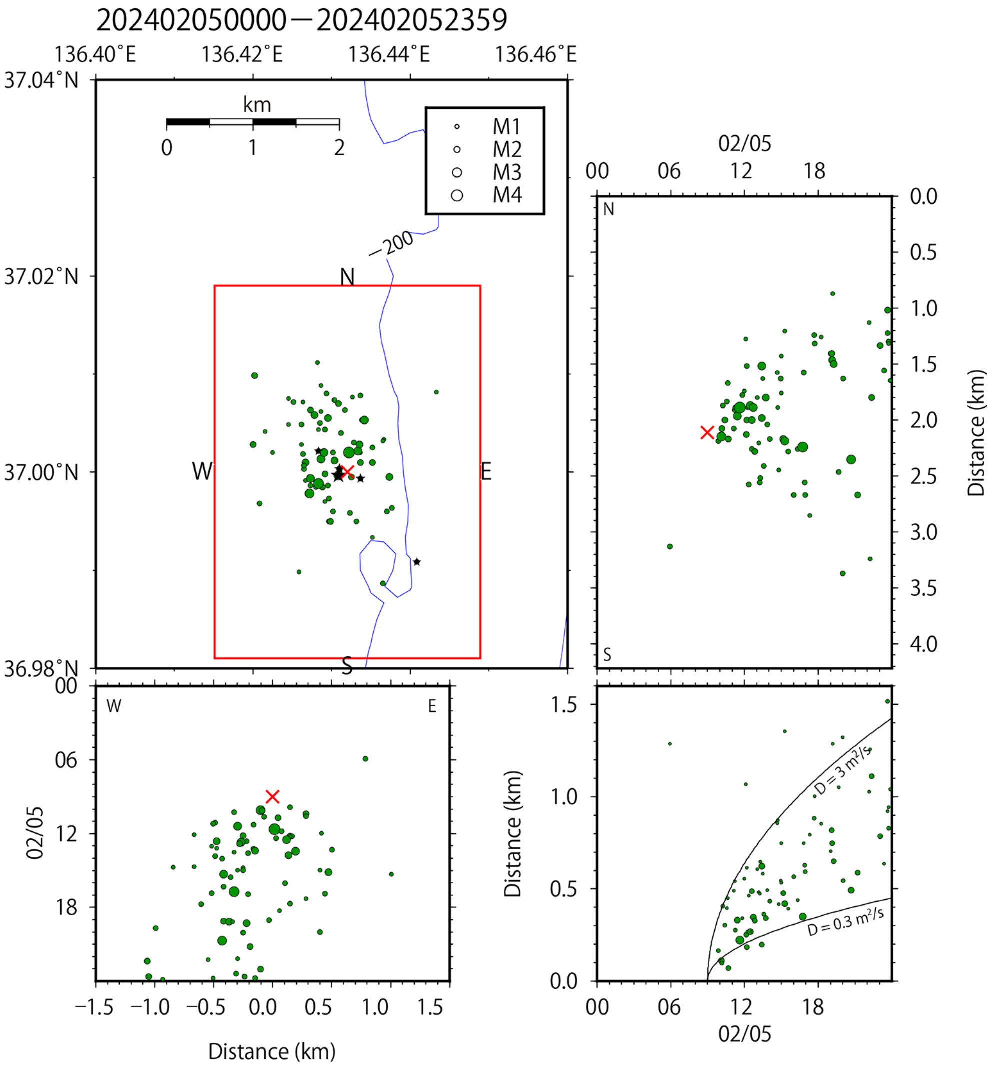

Fig. 8 Same as Fig. 7, but for the activity on 5 February. Location of the starting point (red cross mark) was determined similarly to the activity on 26–27 January. The first five earthquakes after 9 a.m. are plotted as black stars in the epicentral map.

sivity of ~1 m^2/s. We selected the starting point of the diffusive activity at a nearly central point in the epicentral distribution of the first five earthquakes after 6 p.m., also referring the north-south and east-west space-time distributions of the activity. From the space-time distributions, it is reasonable to assume that migration—but not diffusion—of earthquakes occurred. However, as observed in Electronic Appendix 3, where migration lines are depicted in the distance—time diagram by considering the M 1.2 earthquake at around 6 a.m. as the starting point, the migration feature becomes very obscure since earthquakes before 6 p.m. are sparse and spread beyond the migration lines.

Fig. 8 is the same as Fig. 7, but for the activity on 5 February. In this case the diffusive feature is clearer. The diffusivity was estimated at ~3 m^2/s. where the starting point was selected using the same procedure used to assess diffu-

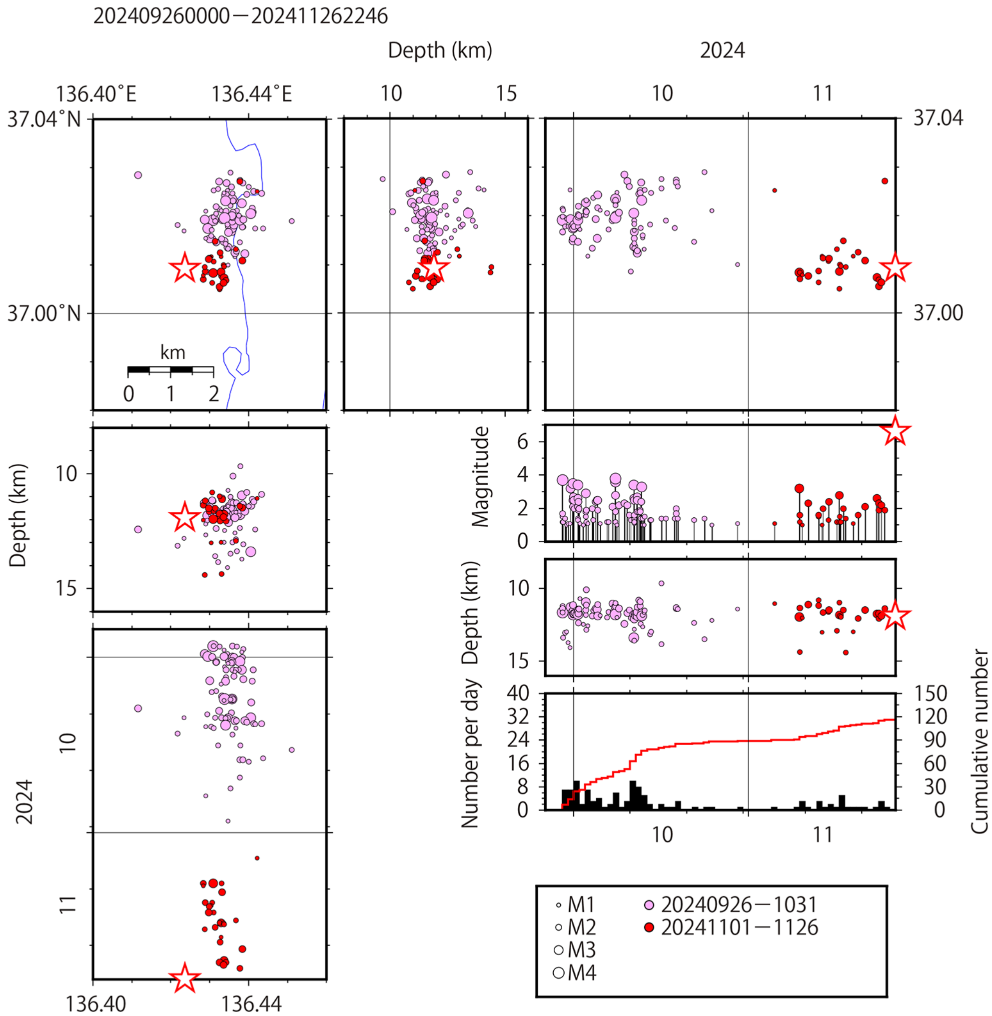

Fig. 9 Same as Fig. 6, but for activities in Periods 3 and 4. Earthquakes in Periods 3 and 4 are plotted in pink and red, respectively. The red star represents the hypocenter of the *M* 6.6 earthquake inferred from differences in DPAT between the *M* 6.6 earthquake and the *M* 3.2 and *M* 4.0 events（cf. Fig. 5）.

sive activity on 26–27 January. In Electronic Appendix 4, diffusion curves are fitted when different times are used as the starting point.

2）Activity in Period 2

In Period 2, earthquakes occurred rather sparsely around the area of activity in Period 1. No short-time swarm-like activity was observed.

3）Activity in Periods 3 and 4

Fig. 9 shows epicentral distribution, cross sections and space-time distributions in the north-south and east-west directions, and an M-T diagram, change in depth and daily and cumulative number of earthquakes in Periods 3 and 4. Activities in these periods occurred in an elliptical area of around 3 km × 1.5 km with its major axis running in an NNE-SSW direction. The area of activity in Period 4, which was located south of the activity in Period 3, overlaps with the area of activity in the latter half of Period 1. However, the depths of earthquakes in the two periods differed: earthquakes in Period 4 occurred in a shallower layer than earth-

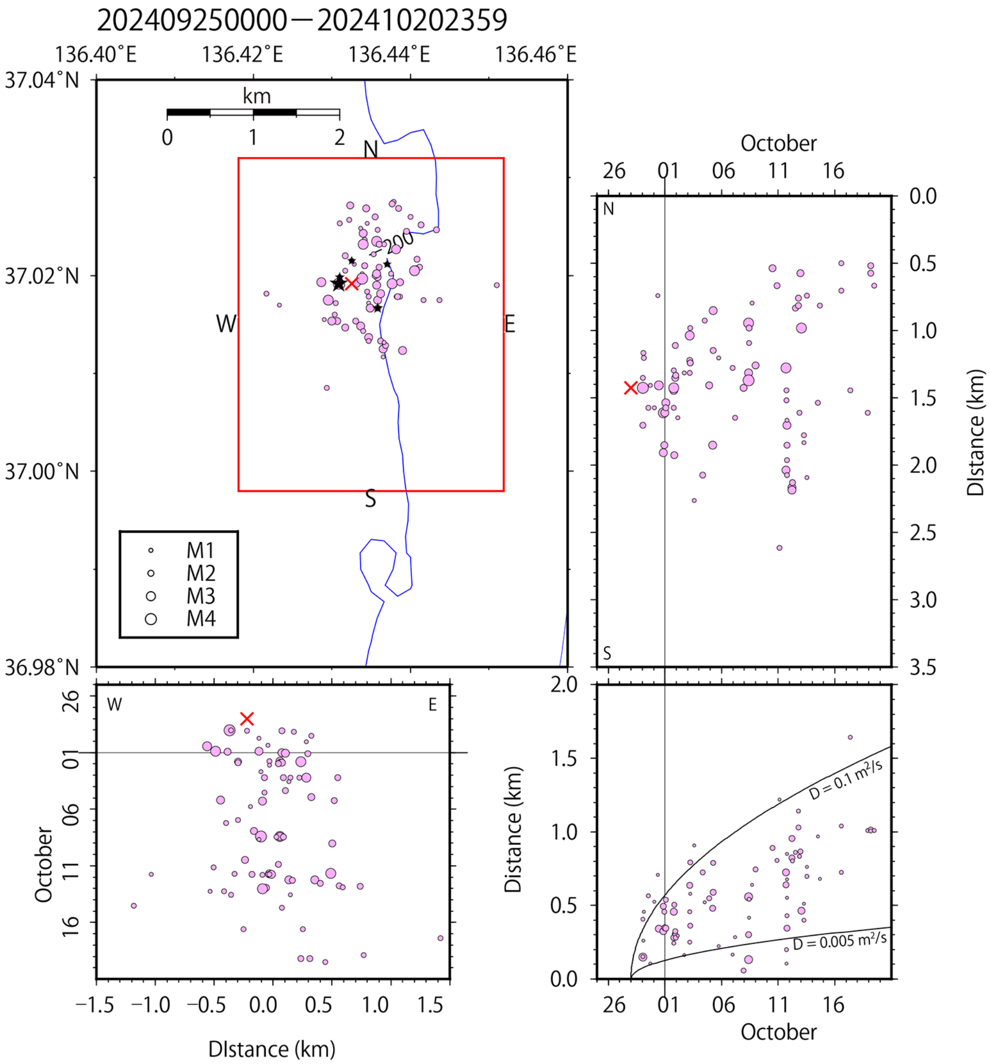

Fig. 10 Same as Fig. 7, but for the activity in Period 3. The area of activity spread at a diffusivity of 0.005 m^2/s. Location of the red cross mark was determined similarly to the activities in Period 1. The first five earthquakes that occurred after 28 September are plotted as black stars in the epicentral map.

quakes in Period 1 (see Fig. 2). The star in Fig. 9 represents the estimated hypocenter of the M 6.6 earthquake (see Fig. 5). It is notable that the hypocenter was located near the area of activity in Period 4.

Fig. 10 is the same as Figs. 7 and 8, but for Period 3. If we assume the zero hour of 28 September as the time of commencement of diffusive migration of earthquakes and the cross on the epicentral map as the starting point, it can be observed that the seismicity area spread at a diffusivity of 0.1 m^2/s, although earthquakes occurred persistently around the starting point. The diffusive feature of the seismicity when the commencement was assumed on different days is shown in Electronic Appendix 5.

In the activity of Period 4, seismicity diffused also at a slightly smaller diffusivity (0.05 m^2/s) than that observed in Period 3 (Fig. 11). Electronic Appendix 6 shows the feature of migra-

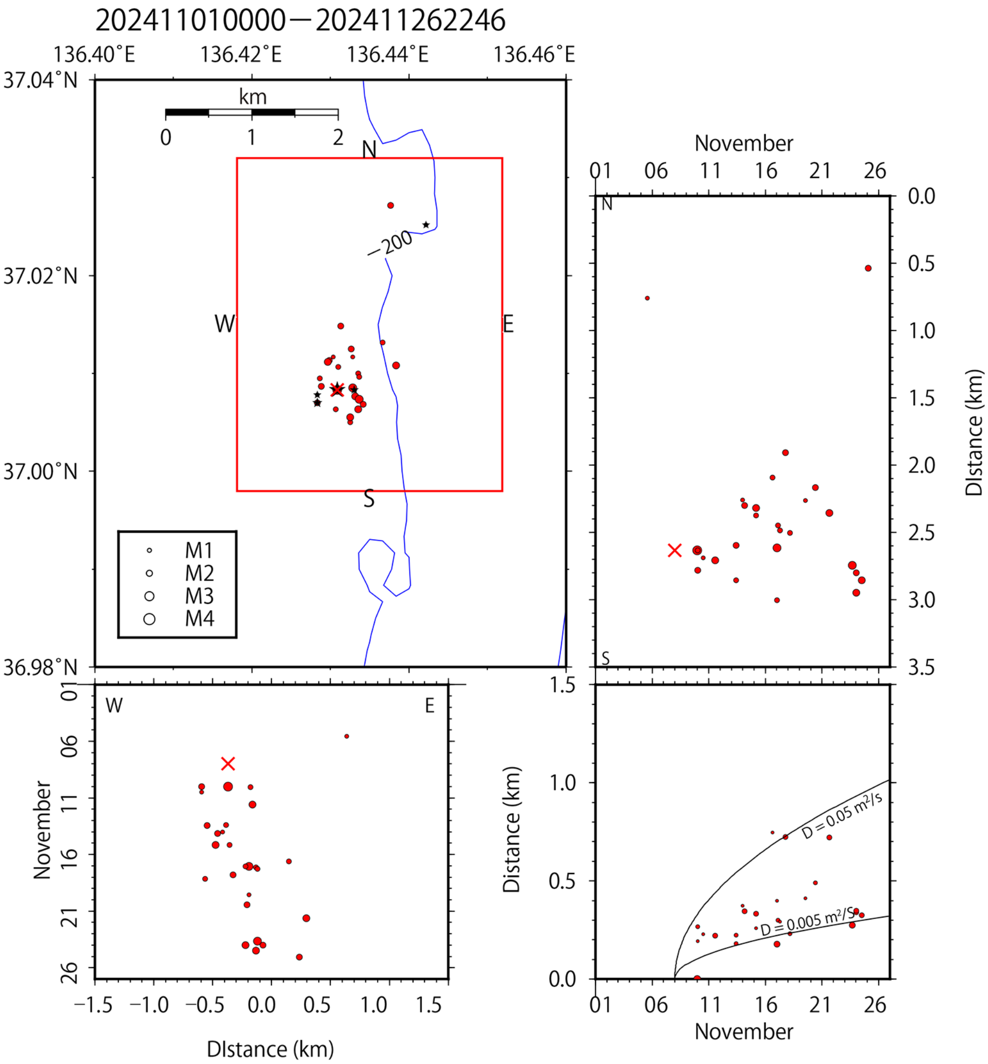

Fig. 11 Same as Fig. 10, but for the activity in Period 4. The area seems to have spread at about 0.005 m^2/s, slightly less than the diffusivity observed in the activity in Period 3. The location of the red cross mark was determined similarly to the activity in Period 3. The first five earthquakes that occurred after 8 November are plotted as black stars in the epicentral map.

tion with diffusion curves when the migration starting time was assumed on different days.

4) Relationship among activities of different periods and aftershock activity

The diffusive migration of earthquakes observed in Period 1 ceased within several hours to half a day. On the other hand, expansion of the seismicity area seen in Periods 3 and 4 continued for more than two weeks and diffusivity was one-order smaller than that observed in Period 1. The inverse relationship between diffusivity and duration is in agreement with the results of a previous study (Amezawa *et al.*, 2021).

We noted that the epicentral area of activity in Period 4 overlaps with that in the latter half of Period 1, however, depths of earthquakes

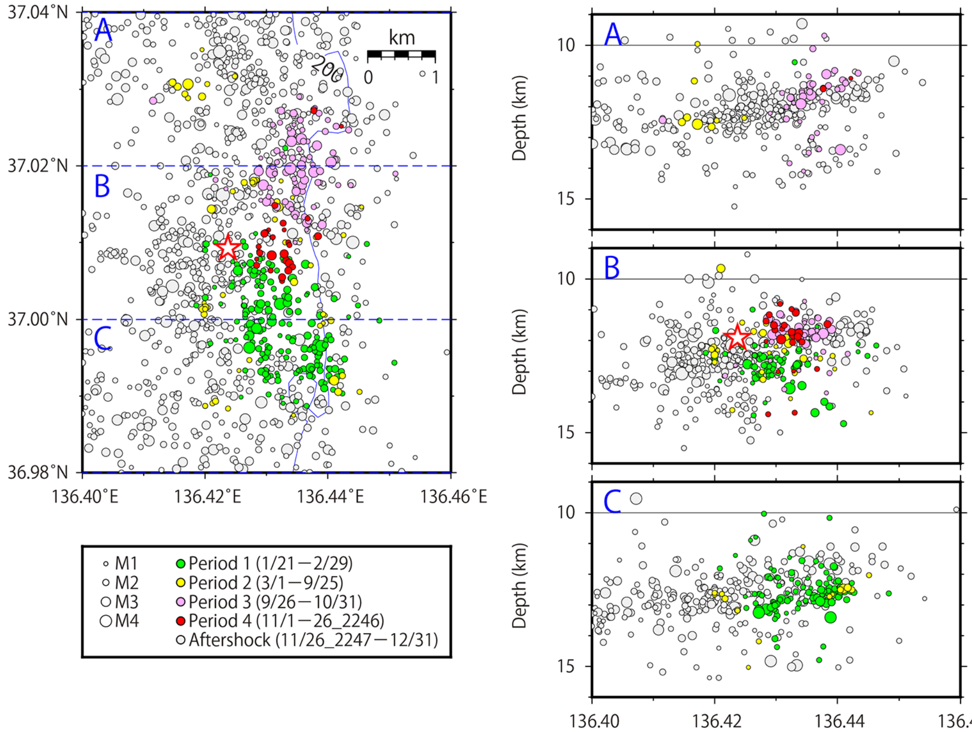

Fig. 12 Epicentral distribution (left panel) and east-west cross sections (right panel) for precursory earthquakes and aftershocks occurred in the period from the mainshock until 31 December 2024. Note that earthquakes in Period 1 occurred in the zone of aftershocks, while earthquakes in Periods 3 and 4 occurred near the upper surface of the aftershock zone. The red star indicates the hypocenter of the M 6.6 earthquake inferred from a comparison of DPAT values (see Figs. 4 and 5).

differed. From cross-sections where hypocenters of precursory earthquakes and aftershocks are superimposed (Fig. 12), it is clear that earthquakes in Period 1 occurred within the aftershock zone, while earthquakes in Period 4 occurred near the upper surface of the aftershock zone.

Fig. 13 compares the epicentral distributions of earthquakes in Periods 1 and 2, and aftershocks of the M 6.6 earthquake. Of note, in the area of activity in Period 1, there were very few earthquakes in Period 2, and aftershocks were also sparce there.

IV. Discussion

Fig. 14 shows magnitude-frequency relationships (Gutenberg and Richter, 1944) for the activities in the entire Periods, in Period 1, and in Periods 3 and 4. The b value, calculated by the formula proposed by Marzocchi and Sandri (2003) using earthquakes with M 1.3 or larger for which almost all earthquakes are considered to be detected, was 0.75 ± 0.07 for Period 1, and 0.53 ± 0.06 for Periods 3 and 4. Scholz (2015) indicated that the b value tends to decrease linearly with an increase in differential stress for both continental crust earthquakes and subduction zone earthquakes. Schorlemmer *et al.* (2005) found that normal faulting earthquakes had the highest b values, thrust earthquakes had the lowest, and strike earthquakes had intermediate b values. Based on the idea that thrust faults tend to be under higher stress than normal faults, they proposed that the b value acts as a stress meter that depends inversely on differential stress. Many laboratory

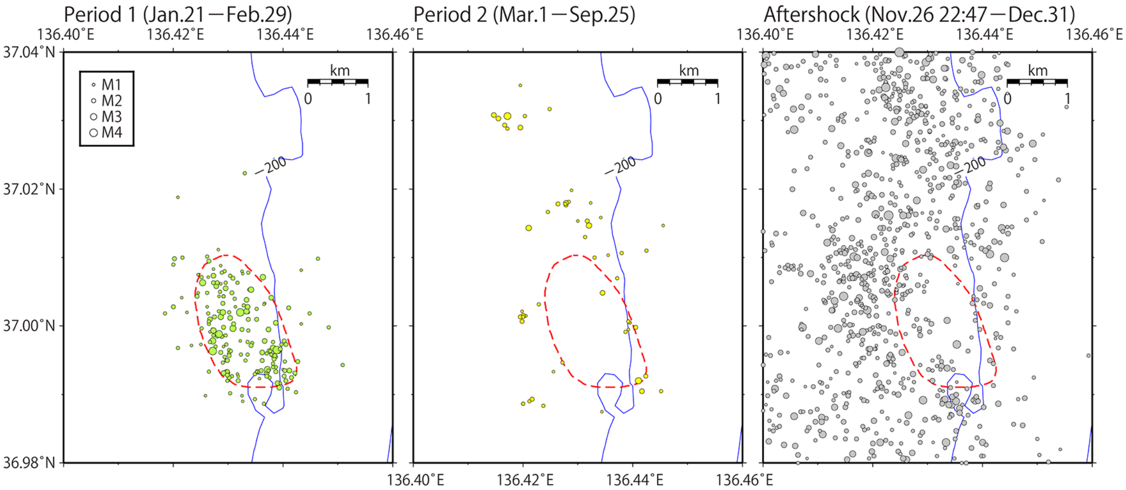

Fig. 13 From left to right, epicentral distribution of earthquakes in Period 1, Period 2 and aftershocks of the M 6.6 earthquake in the period from the mainshock occurrence until 31 December 2024. Location of the ellipse depicted by a broken red line is the same for the three maps.

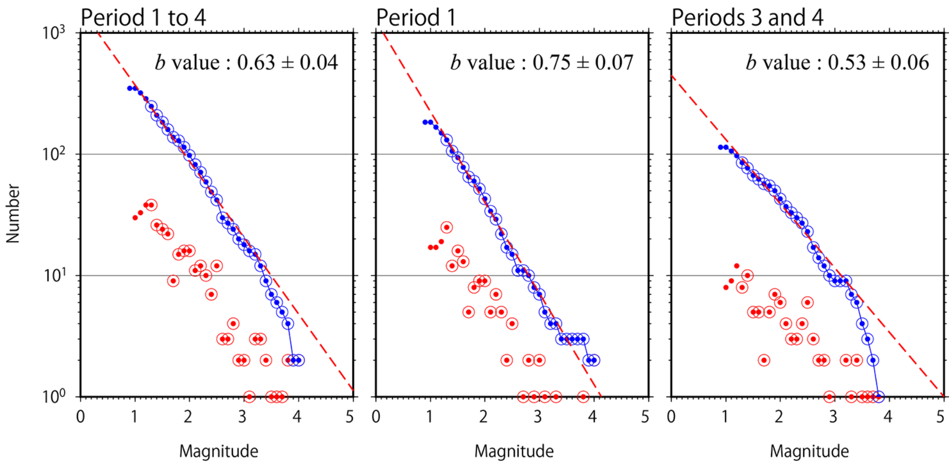

Fig. 14 Magnitude-frequency distributions with a b value (Gutenberg-Richter law) for the whole precursory activity (left), for the activities in Period 1 (middle), and for the activities in Periods 3 and 4 (right). The red and blue dots represent earthquake number in each bin of magnitude and cumulative number of earthquakes, respectively. The b value is calculated by the formula proposed by Marzocchi and Sandri (2003) using number of earthquakes with M 1.3 or larger depicted by red and blue dots with circles. Slope of the dashed regression line corresponds to the b value calculated by the maximum likelihood method.

experiments also showed a decrease in b value with increasing differential stress (e.g., Scholz, 1968; Amitrano, 2003). Considering that b values are supposed to also depend on heterogeneity of the media and confining pressure besides the differential stress (Mogi, 1962; Amitrano, 2003), and that the b value tends to approach the constant 1 when large volumes are sampled (Frohlich and Davis, 1993), a certain b value cannot be correlated with a specific value of differential stress. However, the low b values obtained for the precursory activities indicate that the area was highly stressed, especially in Periods 3 and 4, if these values

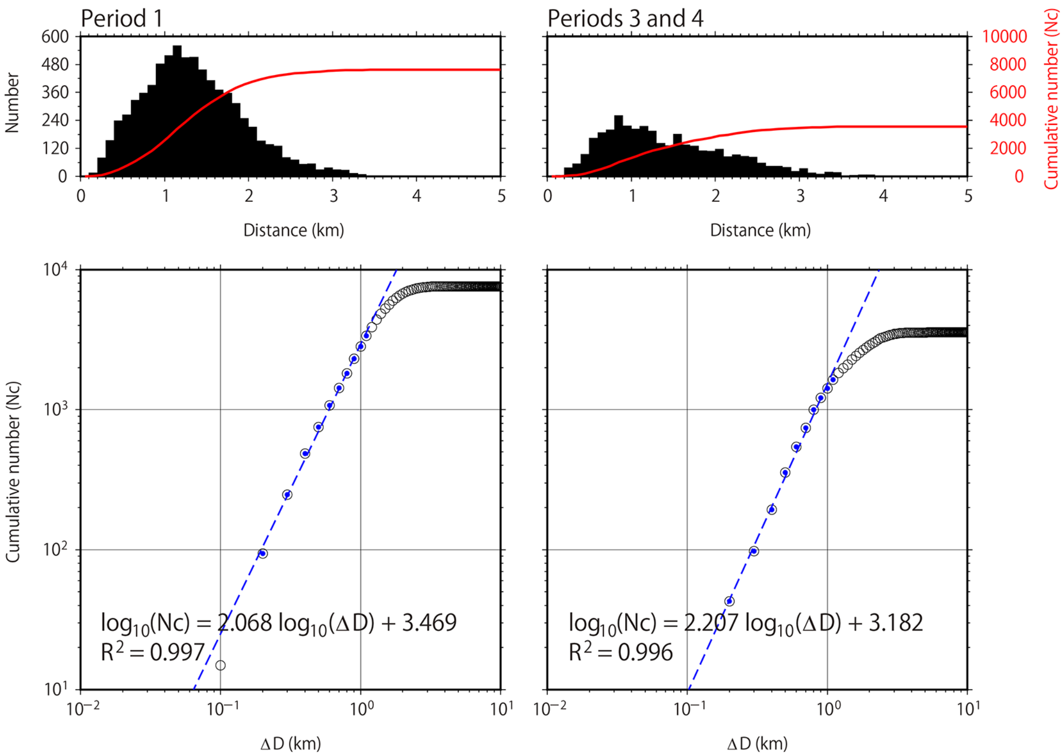

Fig. 15 Top panel: Frequency distribution of hypo-central distances for all pairs of earthquakes with *M* 1.3 or larger in Period 1 (left) and in Periods 3 and 4 (right). The cumulative number of the hypo-central distances is represented by a red curve with a scale on the right side. Bottom panel: The relation between cumulative number of hypo-central distances for all pairs of earthquakes with *M* 1.3 or larger and the distance in Period 1 (left), and in Periods 3 and 4 (right). The ordinate represents the logarithm of cumulative number. The broken line is a least square regression line obtained by using points with a distance less than 1.1 km.

are superimposed on a diagram exhibiting an inverse relationship between *b* values and differential stress (see Fig. 1 in Scholz, 2015).

Fig. 15 shows the relationship between the cumulative number of hypo- central distances for every pair of earthquakes in Period 1 (left panel) and Periods 3 and 4 (right panel). The ordinate of the bottom graphs is the logarithm of the cumulative number of distances for all pairs of earthquakes with *M* 1.3 or larger, and the abscissa is the distance. Note that the logarithm of the cumulative number increases linearly with distance in the range less than 1 km. The slope of the line is considered to represent the fractal dimension of the spatial distribution of earthquakes (Takayasu, 2010). The fractal dimension obtained for the activities in Period 1 is 2.05, while that for the activities in Periods 3 and 4 is 2.21. Considering the relationship between the complexity of the rupture of fault motion (fractal dimension) and the *b* value, Aki (1981) argued that the fractal dimension and *b* value are linearly related. If one considers that the fractal dimension obtained for the spatial distribution of earthquakes reflects complexity of the generation area of earthquakes, then the result, which the fractal dimension for the activities in Period 1 is smaller than that for the activities in Periods 3 and 4, indicates that such a relationship, as suggested by Aki (1981), was not observed in the precursory activity of the *M* 6.6 west-off Noto Peninsula earthquake, because a smaller fractal dimension was obtained for the activities of a larger *b* value. On the other hand, while conducting numerical simulations of the brittle-ductile transition, Amitrano (2003) found that the spatial correlation dimension of damage distribution, D, was negatively correlated with b value. Based on that simulation, Amitrano (2003) suggested that the spatial distribution of localized damage that is related to brittleness is associated with a high b value while the spatial distribution of diffused damage that is related to ductility is associated with a low b value. It may be necessary to reflect further on what the fractal dimension calculated by the spatial correlation of earthquake distribution physically represents.

As depicted in the previous section, each notable seismic activity prior to the M 6.6 earthquake exhibited a diffusive feature. Diffusivity for the activities in Period 1 was estimated at ~1 m^2/s, while that in the Periods 3 and 4 was estimated at ~0.1 m^2/s, i.e., one order smaller. Besides the difference in diffusivity between activities in Period 1 and Periods 3 and 4, differences in their durations were also observed: whereas the activities in Period 1 ceased within several hours to half a day, those of Periods 3 and 4 continued for over two weeks. These differences in diffusivity and duration between the activities in Period 1 and Periods 3 and 4 suggest that the diffusive migration of earthquakes in Period 1 and that in Periods 3 and 4 originated from different causes.

Earthquake migration or diffusion are ubiquitously observed in swarm activities and are generally categorized into two groups: one is linked to aseismic slow slips while the other is related to the diffusion of fluids. In both groups, migration velocity is inversely related to duration, i.e., a shorter duration is associated with a larger velocity, although velocity of the former group is one or two orders larger than that of the latter group (Danré *et al*., 2024). We consider the earthquake diffusion observed in Period 1 with relatively large diffusive velocity and short durations might be caused by slow slips. Our finding that the fractal dimension for spatial distribution of hypocenters is very close to 2 supports the supposition that earthquake diffusion observed in Period 1was linked to an aseismic slow slip. The sparse aftershocks in the area of activities in Period 1 (Fig. 13) suggest that the mainshock fault in the area had slipped somewhat beforehand.

On the other hand, it is noteworthy that the diffusivity of ~0.1 m^2/s is similar to the value of diffusive hypocenter migrations observed in the swarm activity occurring before the 2024 Noto Peninsula earthquake (Amezawa *et al*., 2023). Yoshida *et al*. (2023) proposed that the migration of the earthquakes was caused by the upward intrusion of fluids. The similarity in their diffusivity as well as their comparatively long durations suggest that the seismic activity in Periods 3 and 4 were caused by the percolation of fluids into that area.

Although seismic activity preceding a large earthquake manifests diversity according to the tectonic and seismogenic state of the area around its focus (e.g., Chen and Shearer, 2013; Ruiz *et al*., 2014; Cabrera *et al*., 20221), a low b value is a commonly observed feature in foreshock activities (e.g., Shimbaru and Yoshida, 2021), indicating that the area around the focus of a large earthquake is highly stressed (Scholz, 2015). Another feature of foreshock activities is that they occur in proximity of the hypocenter of a mainshock (Hamada, 1987; Yoshida and Hamada, 1991; Maeda, 1996). We note that the b value of the activity in Period 4 was especially low (Fig. 14) and the activity area was located in the vicinity of the hypocenter of the M 6.6 earthquake. These findings imply that earthquakes in Period 4 were “foreshocks”. It is to be noted that the “foreshocks” occurred near the upper surface of the aftershock zone (Fig. 13).

The seismograms of the M 6.6 west-off Noto Peninsula earthquake show that amplitude of the P-wave was initially small for an earthquake of this magnitude. This feature seems to suggest that fault motion first spread rather slowly over a highly stressed area where fluids had percolated and fault strength as a whole had weakened, i.e., over the area of the preceding seismic activity; then, after having fractured the area, the fault motion extended along a pre-existing fault, which finally resulted in the M 6.6 earthquake.

V. Summary

The space-time distribution of seismicity preceding an M 6.6 earthquake that occurred west-off the Noto Peninsula on 26 November 2024 was investigated using a hypocenter catalogue relocated based on waveform correlation. Short-term activities of several hours to half a day were observed in the period from late January until mid-February (Period 1), while relatively long-term activities of about two weeks were observed in the periods from late September until October (Period 3) and from the beginning of November until the occurrence of the M 6.6 earthquake (Period 4). Over about half a year, between early March until late September (Period 2), seismicity was inactive. In each of the active Periods diffusive earthquake migration was observed. Diffusivity was estimated at about 1 m^2/s for the activities in Period 1, and about 0.1 m^2/s, one-order smaller, for the activities in Periods 3 and 4. The value of diffusivity and their short duration suggest that the migration phenomena in Period 1 were linked with slow slips. This supposition is supported by the fractal dimension of the hypocenter distribution in Period 1, which is nearly 2.0. On the other hand, diffusivity in Periods 3 and 4 is almost the same as that observed in swarm activity before the M 7.6 Noto Peninsula earthquake. Based on similar diffusivity, and by their relatively long duration, the diffusive migration of earthquakes in Periods 3 and 4 may have been caused by the intrusion of fluids.

The b value of precursory activity—especially of the activity in Period 4 which occurred in the proximity of the hypocenter of the M 6.6 earthquake—was very low, indicating that the area was highly stressed. The amplitude of the P-wave of the M 6.6 west-off Noto Peninsula earthquake was rather small initially and gradually grew. The fault motion may have begun to spread rather slowly over an area where fluids had percolated and fault strength overall had weakened, i.e., over the area of the preceding seismic activity. Thereafter, having fractured the area, the fault motion extended along a pre-existing fault, which finally resulted in the M 6.6 earthquake.

Acknowledgement

We are grateful to two anonymous reviewers whose comments were very helpful to improve the manuscript. We used seismic data observed by high sensitivity seismographs from the following sources: National Research Institute for Earth Science and Disaster Resilience (2019), Kyoto University, and JMA. To collect the necessary data, we used the large continuous seismic data analyzing system (Nakagawa *et al.*, 2016) of the Earthquake Research Institute at the University of Tokyo. We used the JMA unified catalog[1]. We used GrowClust (Trugman and Shearer, 2017) to estimate precise hypocenter locations. We used Generic Mapping Tools (Wessel *et al.*, 2013) to create the figures.

Note

1) JMA unified catalog https://www.data.jma.go.jp/svd/eqev/data/bulletin/index.html [Cited 2025/10/16].

References

Aki, K. (1981): A probabilistic synthesis of precursory phenomena. in *Maurice Ewing Series 4, Earthquake Prediction, An International Review* edited by Simpson, D.W. and Richards, P.G., American Geophysical Union, 566–574.

Amezawa, Y., Maeda, T. and Kosuga, M. (2021): Migration diffusivity as a controlling factor in the duration of earthquake swarms. *Earth, Planets and Space*, **73**, 1–11, doi:101186/s40623-021-01480-7.

Amezawa, Y., Hiramatsu, Y., Miyakawa, A., Imanishi, K. and Otsubo, M. (2023): Long-living earthquake swarm and intermittent seismicity in the northeastern tip of the Noto Peninsula, Japan. *Geophysical Research Letters*, **50**(8), e2022GL102670, doi:10.1029/2022GL102670.

Amitrano, D. (2003): Brittle-ductile transition and associated seismicity: Experimental and numerical studies and relationship with the b value. *Journal of Geophysical Research*, **108**, 2044, doi:10.1029/2001JB000680.

Beyreuther, M., Barsch, R., Krischer, L., Megies, T., Behr, Y. and Wassermann, J. (2010): ObsPy: A Python toolbox for seismology. *Seismological Research Letters*, **81**, 530–533, doi:10.1785/gssrl.81.3.530.

Cabrera, L., Poli, P. and Frank, W.B. (2022): Tracking the spatio-temporal evolution of foreshocks preceding the M_w 6.1 L'Aquila earthquake. *Journal of Geophysical Research*, **127**, e2021JB023888, doi: 10.1029/2021JB023888.

Chen, X. and Shearer, P.M. (2013): California foreshock sequences suggest aseismic triggering process. *Geophysical Research Letters*, **40**, 2602–2607, doi: 10.1002/grl.50444.

Danré, P., De Barros, L., Cappa, F. and Passarelli, L. (2024): Parallel dynamics of slow slips and fluid-induced seismic swarms. *Nature Communications*, **15**, 8943, doi:10.1038/s41467-024-53285-3.

Frohlich, C. and Davis, S.D. (1993): Teleseismic b values; or, much ado about 1.0. *Journal of Geophysical Research*, **98**, e2021JB023888, doi:10.1029/2021JB023888.

Gulia, L. and Wiemer, S. (2019): Real-time discrimination of earthquake foreshocks and aftershocks. *Nature*, **574**, 193–200, doi:10.1038/s41586-019-1606-4.

Gutenberg, B. and Richter, C.F. (1944): Frequency of earthquakes in California. *Bulletin of the Seismological Society of America*, **34**, 185–188, doi:10.1785/BSSA0340040185.

Hamada, N. (1987): Re-examination of seismicity associated with destructive inland earthquakes of Japan and its seismological significance. *Papers in Meteorology and Geophysics*, **38**, 77–156, doi: 10.2467/mripapers.38.37. (in Japanese with English abstract)

Japan Meteorological Agency (2024): CMT mechanisms of earthquakes.
https://www.data.jma.go.jp/eqev/data/mech/cmt/top.html [Cited 2025/10/16].

Kato, A., Obara, K., Igarashi, T., Tsuruoka, H., Nakagawa, S. and Hirata, N. (2012): Propagation of slow slip leading up to the 2011 M_w 9.0 Tohoku-ki earthquake. *Science*, **335**, 705–708, doi:10.1126/science.1215141.

Maeda, K. (1996): The use of foreshocks in probabilistic prediction along the Japan and Kuril trenches. *Bulletin of the Seismological Society of America*, **86**, 242–254, doi:10.1785/BSSA08601A0242.

Marzocchi, W. and Sandri, L. (2003): A review and new insights on the estimation of the b-value and its uncertainty. *Annals of Geophysics*, **46**, 1271–1282, doi:10.4401/ag.3472.

Mogi, K. (1962): Magnitude-frequency relation for elastic shocks accompanying fractures of various materials and some related problems in earthquakes. *Bulletin of Earthquake Research Institute*, **40**, 831–853, doi:10.15083/0000033759.

Nakagawa, S., Tsuruoka, H., Kato, A., Sakai, S. and Hirata, N. (2016): A Petabyte-scale large continuous seismic data analyzing system. *Bulletin Earthquake Research Institute*, **91**, 1–9, doi:10.15083/0000032408. (in Japanese with English abstract)

Nanjo, K. and Yoshida, A. (2021): Changes in the b value in and around the focal areas of the M 6.9 and M 6.8 earthquakes off the coast of Miyagi prefecture, Japan, in 2021. *Earth Planets and Space*, **73**, 176, doi:10.1186/s40623-021-01511-3.

Nanjo, K., Hirata, N., Obara, K. and Kasahara, K. (2012): Decade-scale decrease in b value prior to the M9-class 2011 Tohoku and 2004 Sumatora quakes. *Geophysical Research Letters*, **39**, L20304, doi:10.1029/2012GL052997.

National Research Institute for Earth Science and Disaster Resilience (2019): NIED Hi-net. doi: 10.17598/NIED.0003.

Ruiz, S., Metois, M., Fuenzalida, A., Ruiz, J., Leyton, F., Grandin, R., Vigny, C., Madariaga, R. and Campos, J. (2014): Intense foreshocks and a slow slip event preceded the 2014 Iquique M_w 8.1 earthquake. *Science*, **345**, 1165–1169, doi:10.1126/science.1256074.

Scholz, C.H. (1968): The frequency-magnitude relation of microfracturing in rock and its relation to earthquakes. *Bulletin of the Seismological Society of America*, **58**, 399–415, doi:10.1785/BSSA0580010399.

Scholz, C.H. (2015): On the stress dependence of the earthquake b value. *Geophysical Research Letters*, **42**, 1399–1402, doi:10.1002/2014GL062863.

Schorlemmer, D., Wiemer, S. and Wyss, M. (2004): Earthquake statistics at Parkfield: 1. Stationarity of b values. *Journal of Geophysical Research*, **109**, B12307, doi:10.1029/2004JB003234.

Schorlemmer, D., Wiemer, S. and Wyss, M. (2005): Variation in earthquake-size distribution across different stress regimes. *Nature*, **437**, 539–542, doi: 10.1038/nature04094.

Shapiro, S.A., Huenges, E. and Borm, G. (1997): Estimating the crust permeability from fluid injection-induced seismic emission at the KTB site. *Geophysical Journal International*, **131**, F15–lF18, doi: 10.1111/j.1365-246X.1997.tb01215.x.

Shimbaru, T. and Yoshida, A. (2021): The b value in the seismic activity around foci of large crustal earthquakes before and after their occurrence. *Zisin 2*, **74**, 77–86, doi:10.4294/zisin.2020-5. (in Japanese)

Sugan, M., Kato, A., Miyake, H., Nakagawa, S. and Vuan, A. (2014): The preparatory phase of the 2009 M_w 6.3 L'Aquila earthquake by improving the detection capability of low-magnitude foreshocks. *Geophysical Research Letters*, **41**, 6137–6144, doi: 10.1002/2014GL061199.

Takayasu, H. (2010): *Fractal*. Asakura Publishing, 200p. (in Japanese)

Toda, S. and Stein, R. (2024): Intense seismic swarm punctuated by a magnitude 7.5 Japan shock. *Temblor*, doi:10.32858/temblor.333.

Trugman, D.T. and Shearer, P.M. (2017): GrowClust: A hierarchical clustering algorithm for relative earthquake relocation, with application to the Spanish Springs and Sheldon, Nevada, earthquake sequences. *Seismological Research Letters*, **88**(2A), 379–391, doi:10.1785/0220160188.

Ueno, H., Hatakeyama, S., Aketagawa, T., Funasaki, J. and Hamada, N. (2002): Improvement of hypocenter determination procedures in the Japan Meteorological Agency. *Quarterly Journal of Seismology*, **65**, 123–134. (in Japanese with English abstract)

Waldhauser, F. and Ellsworth, W.L. (2000): A double-difference earthquake location algorithm: method and application to the northern Hayward fault, California. *Bulletin of the Seismological Society of America*, **90**, 1353–1368, doi:10.1785/0120000006.

Wessel, P., Smith, W.H.F., Scharroo, R., Luis, J. and Wobbe, F. (2013): Generic mapping tools: improved version released. *Eos, Transactions of the American Geophysical Union*, **94**, 409–410, doi:10.1002/2013EO450001.

Yoshida, A. and Hamada, N. (1991): Redetermination of hypocenters of foreshocks, mainshock, and aftershocks of the Kita-Izu earthquake and the Ito earthquake swarm of 1930. *Journal of Physics of the Earth*, **39**, 329–344, doi:10.4294/jpe1952.39.329.

Yoshida, K., Uchida, N., Matsumoto, Y., Orimo, M., Okada, T., Hirahara, S., Kimura, S. and Hino, R. (2023): Updip fluid flow in the crust of the northeastern Noto Peninsula, Japan, triggered the 2023 M_w 6.2 Suzu earthquake during swarm activity. *Geophysical Research Letters*, **50**, e2023GL106023, doi:10.1029/2023GL106023.

Zhu, W., Mousavi, S.M. and Beroza, G.C. (2019): Seismic signal denoising and decomposition using deep neural networks. *IEEE Transactions on Geoscience, and Remote Sensing*, **57**, 9476–9488, doi:10.1109/TGRS.2019.2926772.

2024年能登半島西方沖の地震（*M* 6.6）に先行した拡散的な地震活動

板　寺　一　洋*　中　村　雅　基**　明田川　　保***
弘　瀬　冬　樹**　吉　田　明　夫*

波形相関に基づいた震源再決定カタログを用い，2024年11月26日に能登半島西方沖で発生した地震（*M* 6.6）に先駆した活動について調査した。先駆的活動は，その時空間分布の特徴から4つの期間に分割できる。Period 1：2024年1月下旬～2月，Period 2：3月～9月下旬，Period 3：9月末～10月末，Period 4：11月初め～*M* 6.6の地震発生まで。この中で，Period 1では短時日の活動の活発化，Periods 3，4では2週間ほど続く活動が観測された。これらのいずれの活動においても，地震発生域が広がっていく拡散現象が観測された。拡散係数はPeriod 1では約1 m^2/s，一方，Periods 3，4の活動では約0.1 m^2/sと一桁小さく見積もられた。拡散現象の継続時間についてはPeriod 1では数時間～半日程度であったのに対して，Periods 3，4では約2週間と長く継続した。拡散係数と継続時間の負の相関は先行研究の指摘と整合する。Period 1の活動で見られた拡散現象はその拡散速度や数時間～半日程度という比較的短い継続時間からゆっくりした断層すべりに伴ったものであると推定される。震源分布のフラクタル次元が2に近い値を示すこともその見方と整合する。一方，Periods 3，4の活動で観測された拡散速度は，2024年能登半島地震（*M* 7.6）に先行した群発活動で見られた拡散現象の速度とほぼ同じであり，破砕帯内への水の浸透によって生じたと考えられる。先行的活動のG-R則の*b*値は低い値を示し，特にPeriods 3，4の活動の*b*値は0.53 ± 0.06と低い値だった。低い*b*値は高応力場であることを示しており，また，先行的活動は*M* 6.6の地震の震源近くで発生したとみられることから，震源付近は地震発生前に高応力場であったと推定される。能登半島西方沖の*M* 6.6の地震の観測波形からは，その規模としては小さな振幅で始まって，次第に振幅が増大していった様子が見てとれる。震源付近で高応力場を支えていた小アスペリティが壊れることによって，水の浸透などによって全体として断層強度が弱化していた先行的地震活動域ですべり運動が生じ，その後，既存断層に沿って破壊が進展・拡大していったと考えられる。

キーワード：2024年能登半島西方沖地震，拡散，波形相関，前震，b-値，フラクタル次元

* 静岡大学防災総合センター
** 気象研究所
*** 大阪管区気象台